Available online at www.sciencedirect.com
ScienceDirect
Acta Materialia 55 (2007) 3929–3942
Acta MATERIALIA
www.elsevier.com/locate/actamat

Strain and texture evolution during mechanical loading of a crack tip in martensitic shape-memory NiTi

M.R. Daymond [a,*], M.L. Young [b], J.D. Almer [c], D.C. Dunand [b]

[a] Department of Mechanical and Materials Engineering, Queen's University, Kingston, Ont., Canada K7L 3N6
[b] Department of Materials Science and Engineering, Northwestern University, Evanston, IL 60208, USA
[c] Advanced Photon Source, Argonne National Laboratory, Argonne, IL 60439, USA

Received 28 February 2007; accepted 11 March 2007
Available online 7 May 2007

Abstract

In situ synchrotron X-ray diffraction measurements are used to create two-dimensional maps of elastic strain and texture, averaged over a compact-tension specimen thickness, near a crack tip in a martensitic NiTi alloy. After fatigue crack propagation, the material ahead of the crack and in its wake exhibits a strong texture, which is eliminated by subsequent shape-memory heat treatment, indicating that this texture is due to detwinning, the main deformation mechanism of NiTi. Upon subsequent application of a static tensile stresses, the highly textured zone reappears and grows around the crack tip as the applied stress is increased. At the highest applied stress intensity of 35 MPa $m^{1/2}$, large tensile strains are measured ahead of the crack tip and considerable elastic anisotropy is observed. This detwinning zone is similar to the plastic zone produced by dislocation slip present around cracks in other metals. The texture in this zone is not significantly altered after mechanical unloading, despite the development of substantial triaxial compressive residual strains in this zone.

Keywords: Nitinol; Ni–Ti; Shape memory; Superelasticity; Smart materials

1. Introduction

Shape-memory alloys (SMA) with near-equiatomic Ni–Ti compositions have found use in a range of technological and engineering applications, owing to their unique transformation-induced shape-recovery capabilities [1,2]. Additionally, their excellent corrosion resistance, biocompatibility, dynamic and static strength, damping capability and radio-opacity have made NiTi-based SMA attractive for medical implants and devices [3–5]. Fundamental to the unusual mechanical properties of NiTi is its thermoelastic, reversible martensitic phase transformation [1]. The cubic parent austenite phase transforms to the monoclinic martensite phase (B19, $a = 2.88$ Å, $b = 4.61$ Å, $c = 4.14$ Å, $\gamma = 96.4°$ [1]) phase upon cooling through the martensite-start (M_s)–martensite-finish (M_f) temperature interval, which is dependent on composition and processing. Since the austenite phase has a higher symmetry than the martensite phase, formation of multiple martensite grains (known as variants) with the same crystalline structure but with different orientations occurs through self-accommodation, forming a twinned structure. If a stress is applied, deformation proceeds by "detwinning" or variant selection of the original twinned structure, where some variants grow at the expense of others by the motion of twin boundaries, allowing a macroscopic shape change without dislocation-slip-based plasticity but with large changes in texture (crystallographic orientation). When the temperature is raised through the austenite-start (A_s)–austenite-finish (A_f) temperature range, these detwinned martensite variants revert to the parent phase. If the system is unconstrained, the macroscopic shape change due to detwinning is recovered, resulting in the so-called shape-memory effect; cooling back below M_f results in the original twinned microstructure. In a constrained system, a stress is

* Corresponding author. Tel.: +1 613 533 2193.
E-mail address: daymond@me.queensu.ca (M.R. Daymond).

1359-6454/$30.00
doi:10.1016/j.actamat.2007.03.013

generated as the material attempts to recover its shape. Conversely, if the austenite is stressed above A_f, the transformation from austenite to martensite can be driven by stress alone, resulting in large deformation strains (up to 8% in tension), occurring at a nearly constant stress. Since the martensite phase is unstable at zero stress above A_f, the reverse transformation occurs on removal of the applied stress, resulting in a recovery of deformation; this is known as the superelastic effect.

While the simple macroscopic uniaxial shape-memory and superelastic properties of NiTi are fairly well characterized at the macro- and microscopic levels, and while macroscopic studies of fracture and fatigue in NiTi have been carried out (e.g. [6–13]), there is little microstructural and micromechanical understanding of the effect of detwinning or stress-induced transformation (and the related strain recovery on heating or unloading) upon crack propagation in NiTi, except for some theoretical studies [14–16]. Such microstructural and micromechanical information can be accessed through *in situ* neutron or X-ray diffraction measurements as a function of applied load, as demonstrated by various authors who studied the deformation mechanisms responsible for the shape-memory effect [17–20] and superelasticity [21–28] in NiTi. These studies considered the spatially averaged response of NiTi under simple uniaxial loading. However, the small spot size available with synchrotron X-rays raises the possibility of the spatial mapping of such phenomena, as recently demonstrated by Mehta et al. [29].

We report here *in situ* synchrotron X-ray diffraction mapping of the complex strain and texture field around a sharp fatigue crack tip subjected to a far-field stress. Synchrotron strain measurements around cracks have previously been reported in, e.g., aluminum alloys [30,31] and steels [32,33]. The diffraction data thus obtained allows, in addition, monitoring of the influence of the crack tip stress field on the preferred orientation (i.e. variant selection by detwinning) within monoclinic, martensitic NiTi. In conventional polycrystalline metals, dislocation slip occurs once the local effective stress around the crack tip exceeds the yield stress, resulting in plastic flow and stress redistribution. The goal of our work is to understand the extent to which detwinning occurring in martensitic NiTi can act as an alternative method of relieving the stress field around the crack tip. This information is required to understand the fatigue and fracture behavior of these materials and at present is principally investigated through numerical modeling (e.g. [14–16]).

2. Experimental procedures

Polycrystalline NiTi plates were fabricated by electrodischarge machining (EDM) of a billet previously produced by hot isostatic pressing (HIP) of pre-alloyed NiTi powders (99.9% pure, 49.4 at.% Ni) [18]. The billet had a nominal grain size of 11 ± 3 μm and a random initial texture [18]. To remove any initial residual strains, the material was solutionized at 930 °C for 1 h in titanium-gettered argon and then furnace-cooled to room temperature. This ensured that the material was fully martensitic, given the martensite transformation temperatures ($M_s = 49$ and $M_f = 35 \pm 2$ °C) and austenite transformation temperatures ($A_s = 66$ and $A_f = 86$ °C) reported in Ref. [18].

The plates were then machined into a compact-tension specimen with 3.5 mm thickness and a 17 mm deep notch was cut using EDM, from which a 12 mm long fatigue crack was grown with a nominal ΔK_I of 30 MPa $m^{1/2}$ over 2000 cycles ($R = 0$) at 1 Hz. Based on the requirements of ASTM E399 for fracture toughness testing, the thickness of material required for plane-strain conditions to dominate is $B \geqslant 2.5(K_I/\sigma_{ys})^2$. This condition is an empirical approximation to the requirement that the plastic zone be small compared to the thickness of the sample. Under uniaxial loading conditions, detwinning in this material initiates at an applied stress of around 150 MPa and finishes at approximately 300 MPa, while slip-based plasticity occurs at a stress of around 600–700 MPa, as reported in Refs. [18,34]. Thus, by taking the "yield stress" in the ASTM equation to mean, in this case, the occurrence of detwinning, the dimensions of the sample are such that the sample is not under plane strain conditions, although it is under plane strain conditions if the yield stress appropriate for slip-based plasticity is used instead. However, the sample thickness was constrained to a maximum of 3.5 mm due to the limitations in the penetration depth of X-rays and the experimental arrangements, and thus while we report the nominal applied stress intensity K_I based on plane strain assumptions, the actual K_I imposed will be slightly lower due to the reduced constraint of the thinner samples used, and could be calculated using numerical approaches.

High-energy X-ray diffraction measurements were carried out at the 1-ID beamline of the Advanced Photon Source (Argonne National Laboratory, IL). A tensile force was applied to the specimen using a custom-built, screw-driven loading system mounted on top of a motorized translation table. The system, which is similar to that used in Refs. [35,36], was operated in displacement control, with the macroscopic force applied to the sample recorded using a load cell in the load train. Diffraction measurements were performed with a monochromatic 81 keV ($\lambda = 0.015$ nm)

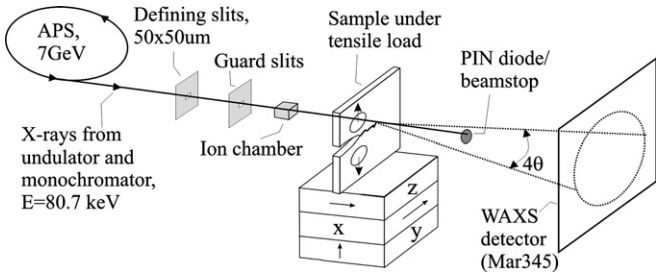

Fig. 1. Schematic illustrating the experimental arrangement and the coordinate system.

X-ray beam in transmission geometry for 30 s. We define the "x" coordinate axis as parallel to the crack growth direction and the "y" coordinate axis as perpendicular to the crack direction but still in the plane of the plate, i.e. parallel to the applied load direction (see Fig. 1). The sample was positioned such that the incident X-ray beam, with a square 50×50 μm^2 cross-section, penetrated the sample parallel to the plate normal direction (Fig. 1). By translating the sample in the x- and y-directions in a raster fashion, diffraction patterns were obtained for various volumes in the vicinity of the crack, building up a spatial diffraction map. Complete Debye–Scherrer diffraction rings from the NiTi present in the $0.05 \times 0.05 \times 3.5$ mm^3 diffraction volume were recorded using an image plate (Mar345) of 345 mm diameter and 100 μm pixel size and with a 16-bit dynamic range. An ion chamber and a PIN (p-type, intrinsic, n-type) diode embedded within the beam stop were used to measure the initial and transmitted intensity, facilitating orientation of the sample, and in particular crack, with respect to the beam. The sample-to-camera distance was ~1.2 m. In addition, calibration diffraction cones were produced from a paste composed of vacuum grease and pure ceria powder (CeO_2, NIST Standard Reference Material SRM-674a), which was smoothly applied to the side edge (yz, Fig. 1) of the sample and measured after each raster. The calibration diffraction data provide a precise conversion between pixel position on the camera and d-spacing of the diffraction peak.

The sample was first measured in the as-fatigued condition, with no applied load. It was then heat-treated outside the beam at 150 °C for 15 min (in the austenitic field, but well below the temperature required for any recrystallization) and then furnace-cooled to room temperature, before again being measured under zero applied load. The load was then increased to four levels ($P = 2.0$, 2.55, 3.05 and 3.55 kN, corresponding to nominal stress intensities $K_I = 20$, 25, 30 and 35 MPa m$^{1/2}$) with raster maps taken at each applied load. The sample was subsequently unloaded and another strain map taken. Finally, another ex situ heat treatment was carried out at 150 °C for 15 min and the sample was measured for a last time. For each measurement, the beam was rastered by translating the sample in the x- or y-direction, using 50 μm steps within 1 mm of the crack tip and larger steps further away, obtaining a total of 200–500 measurement points, as illustrated in Fig. 2. For some data sets, due to limited experimental time, only the inner parts of the map were used, as can be seen on the contour plots shown. The time taken for

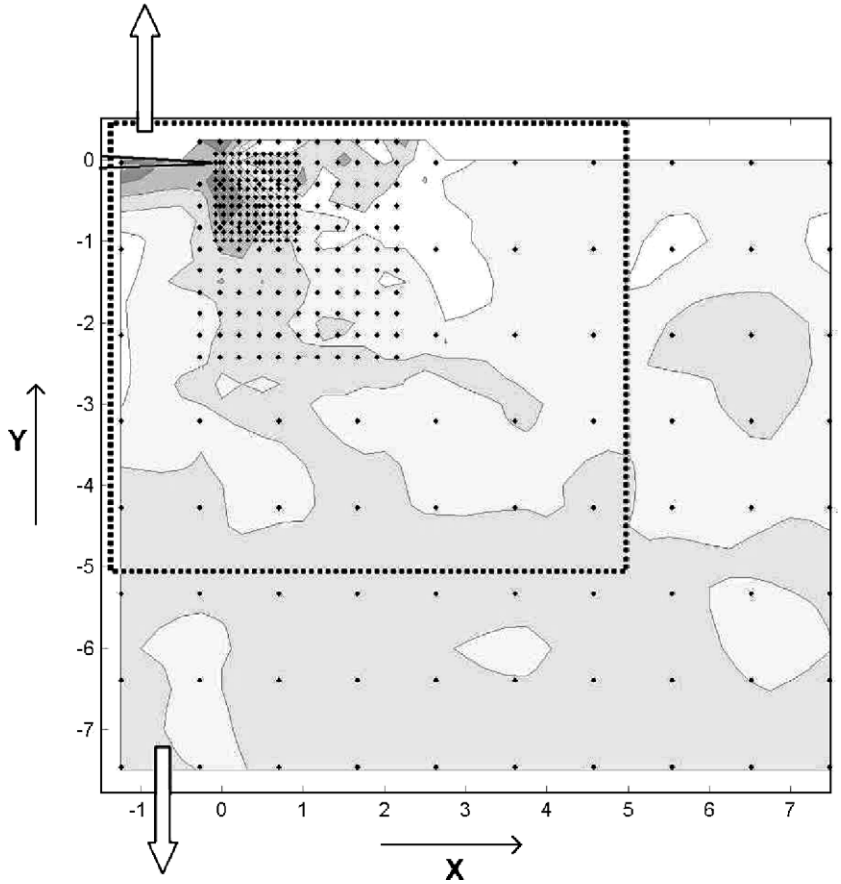

Fig. 2. Illustration of locations at which diffraction measurements were made, with illustrative contour plot data in faint (corresponding to the data shown in Fig. 7a). The crack tip position, as determined by radiography-type intensity scans, is at the origin (0,0), with all dimensions in mm. The far-field uniaxial stress is parallel to the y-direction, as indicated by the large arrows. Although all measured data are used to generate the contour plots, only a central region, as shown by the dotted square, is given in the following figures.

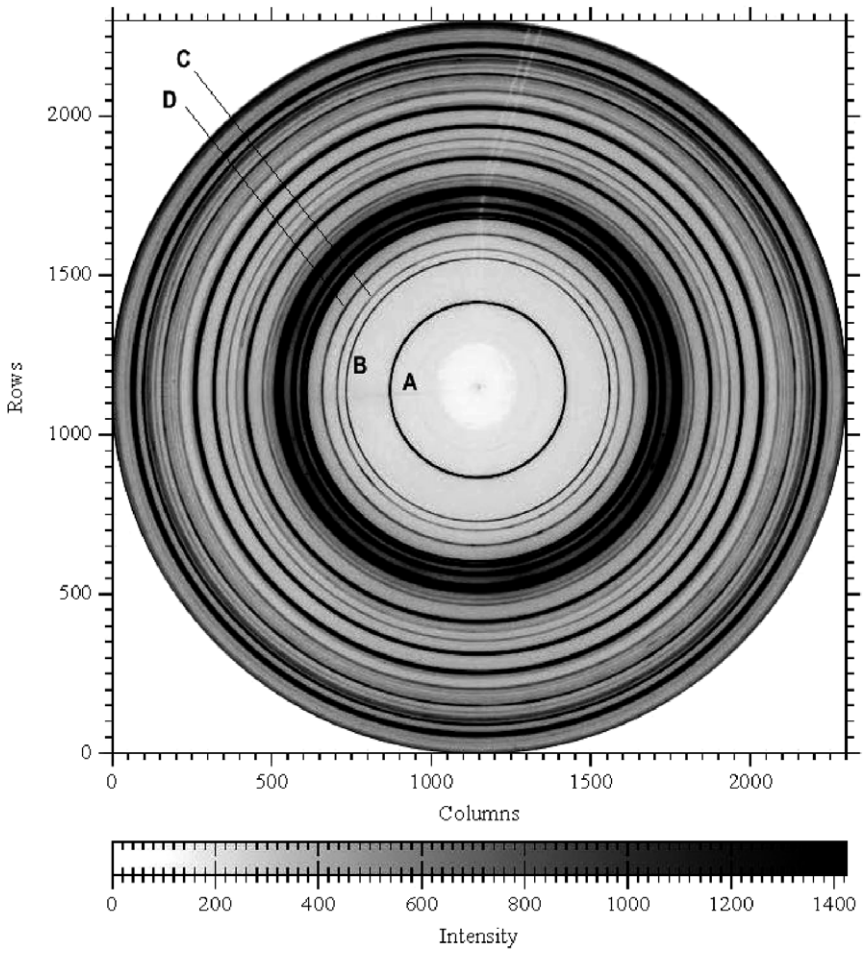

Fig. 3. Typical powder diffraction ring pattern collected far from the crack tip on the as-fatigued sample, at zero applied load. The labels correspond to A – (010), B – (011), C – (100), D – (110) diffraction peaks.

a single map at a given applied load (including readout time and translation) was 8–12 h.

A typical diffraction pattern is shown in Fig. 3, where the rings corresponding to the (010), (011), (100) and (110) reflections are labelled. As evidenced by the smoothness of the diffraction ring intensities, the grain size is significantly smaller than the diffracting volume and the texture is insignificant, providing good polycrystalline averages. To determine the lattice strains from measured diffraction rings, a procedure similar to those from Refs. [36,37] is used, although, due to space restrictions, we report just a subset of the data obtained. This algorithm [38] is implemented using the program language MATLAB [39], and consists of the following steps:

1. The beam center, detector tilt, and sample-to-detector distance ("calibration parameters") are determined with the software FIT2D [40], using CeO_2 (200) reflections near the detector center and CeO_2 (333) reflections near the detector outer edge.
2. The diffraction pattern is converted from polar to Cartesian coordinates in N radial x M azimuthal bins (in this case with values of $N = 500$ over the d-spacing range 1.82–5.05 Å, and $M = 36$, corresponding to an angular increment of 10°) using the calibration parameters to correct for beam center, detector tilt, and sample-to-detector distance. Here, only the patterns near 0°, 90°, 180° and 270° (integrated over ±5° around the nominal direction) are used, corresponding to intensities and strain components ε_{xx} and ε_{yy}, parallel and perpendicular to the crack growth direction, respectively (Fig. 2).
3. The pattern is converted to a GSAS format [41]. Together with the information from the CeO_2 powder which allows a conversion between pixel position and absolute d-spacings, this program is used for single peak fits using an appropriate peak shape (in this case a pseudo-Voigt function). Rietveld [42] refinement of the diffraction pattern would also be possible but was not attempted here.
4. Lattice strains ε_{xx} and ε_{yy} are then calculated as $\varepsilon = (d - d_0)/d_0$, where d_0 is a reference lattice spacing (discussed below), by fitting a peak to the azimuthal diffraction pattern that corresponds to the required direction in the sample. Since the 0° and 180° diffraction patterns are equivalent directions in the sample, the average obtained from analysis of these two patterns is

then reported here as the strain in the x-direction (ε_{xx}) in the sample at that location, and similarly for the 90° and 270° diffraction patterns, which correspond to the y-direction strains ε_{yy}. We observed that the same strain results were obtained for the two equivalent directions (0°/180° and 90°/270°), within experimental error.

5. Integrated intensities and widths for each peak are also determined during the above fitting process, based on the peak parameter values reported from the peak fitting routine. The background intensity contribution is determined by a linear fit over the entire fitted diffraction spectra. The resultant data are then plotted in the form of a two-dimensional map using MATLAB [39].

3. Results

Since the experiment is carried out in transmission, the diffraction pattern obtained is an average of the entire through-thickness material, i.e. $50 \times 50 \times 3500\ \mu m^3$. Thus, the strains or intensities obtained by analysis of the diffraction peaks are averaged over this full thickness. This fact should be considered in interpreting the results presented here since the crack front is unlikely to be completely linear. Furthermore, the stress state will vary from plane-stress at the sample surface to a more complex, perhaps even plane-strain, state near the center of the sample, and the results reported are an average over these stress conditions.

The results reported here include the integrated intensity of various diffraction peaks, as well as the average lattice strains for selected peaks. To allow easy comparisons between different diffraction peaks, a single reference integrated intensity was defined for each diffraction peak by averaging over the entire set of measurements obtained on the sample that had undergone a heat treatment to reproduce the initial near-random texture (e.g. the average of all the values shown in Fig. 5a). All intensities reported have been normalized with respect to the reference intensity for the given diffraction peak and, therefore, do not include

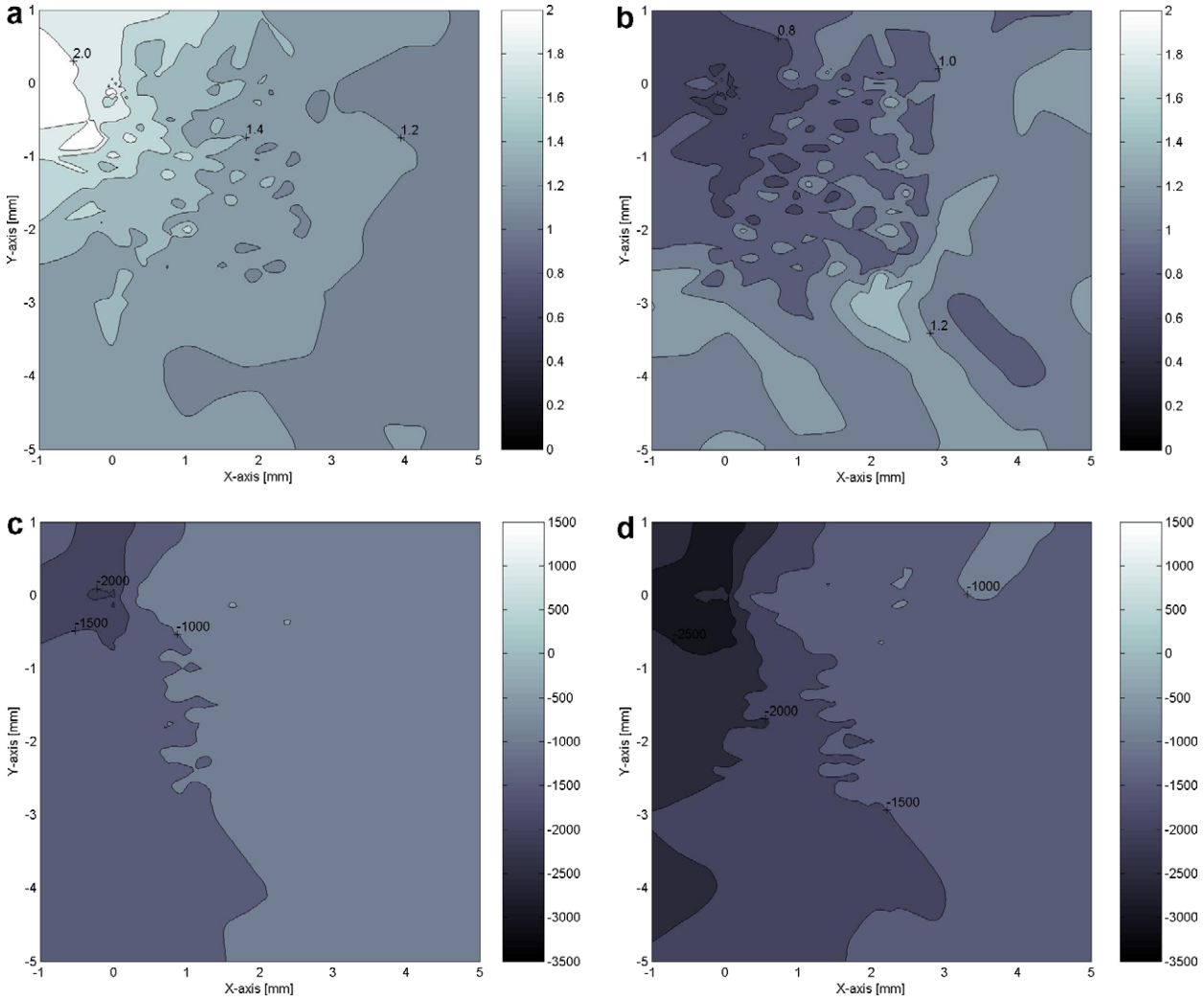

Fig. 4. Texture and strain maps for as-fatigued sample. Normalized intensity parallel to y-direction (perpendicular to crack propagation direction) for (a) (010) peak and (b) (100) peak. Strain component ε_{yy} ($\mu\varepsilon$) for (c) (010) peak and (d) (100) peak.

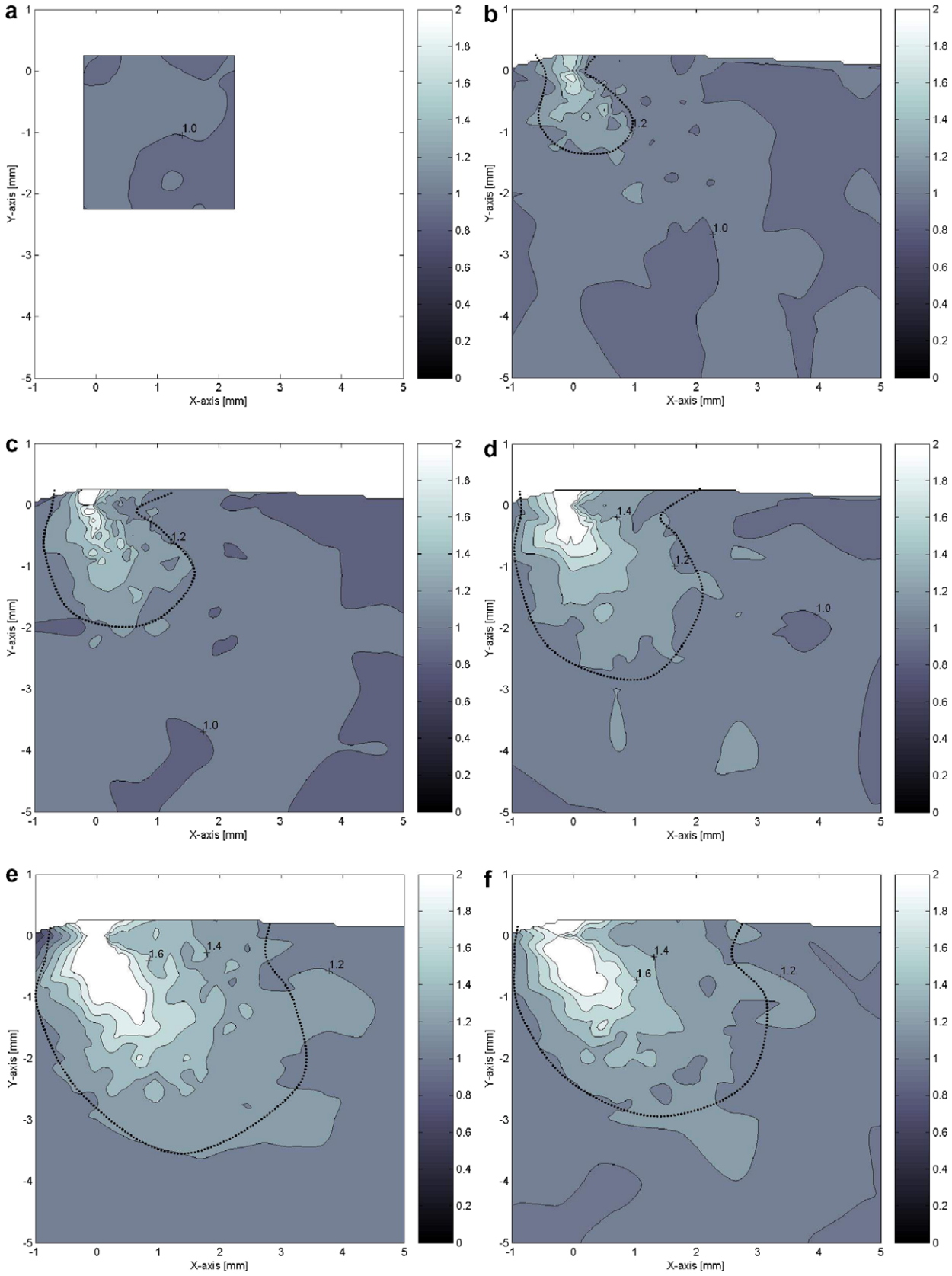

Fig. 5. Evolution of texture maps showing (0 1 0) normalized peak intensity parallel to the y-direction (perpendicular to crack growth) for various K_I values (in MPa $m^{1/2}$): (a) 0, (b) 20, (c) 25, (d) 30, (e) 35, (f) 0 (unload).

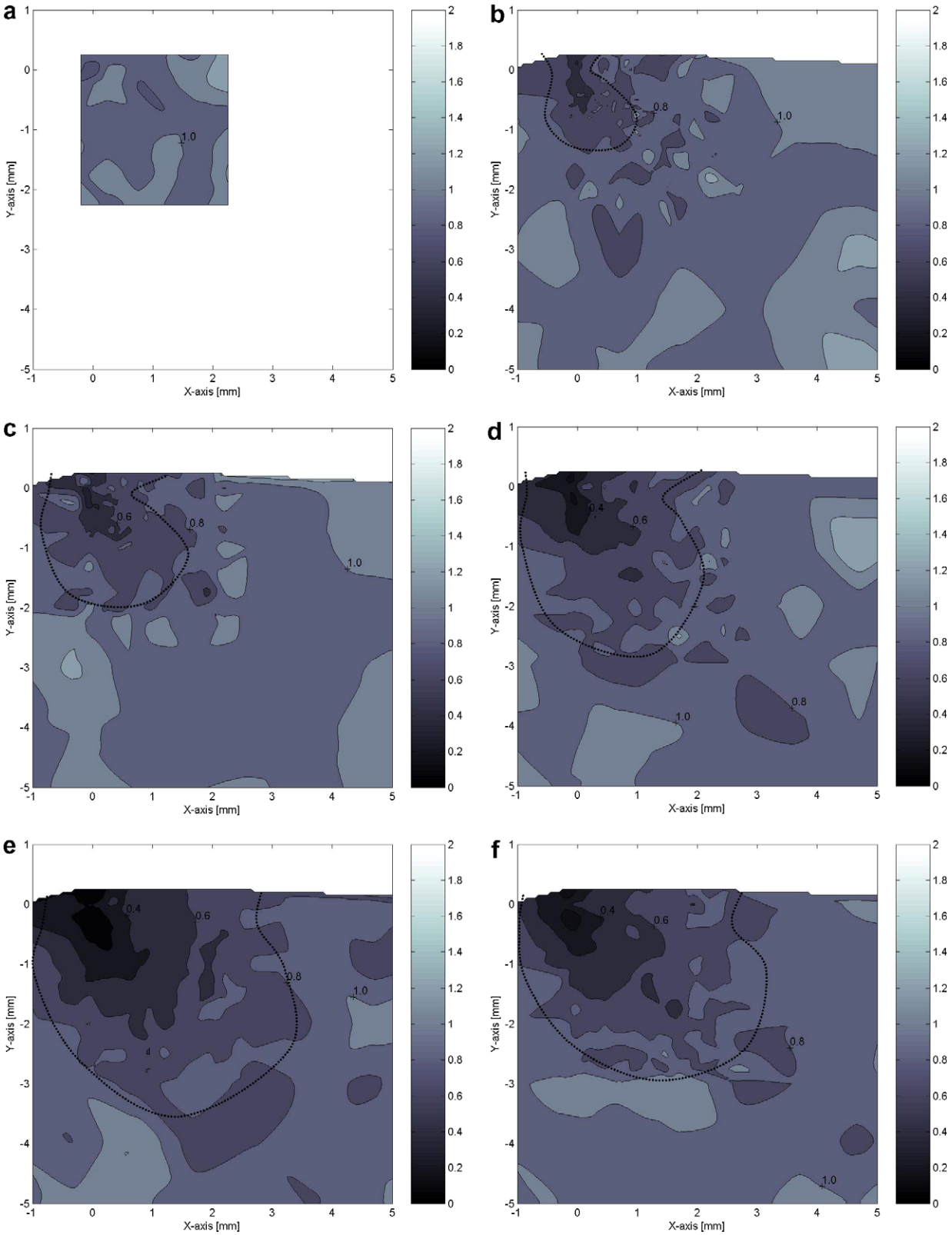

Fig. 6. Evolution of texture maps showing (100) normalized peak intensity parallel to the y-direction (perpendicular to crack growth) for various K_I values (in MPa $m^{1/2}$): (a) 0, (b) 20, (c) 25, (d) 30, (e) 35, (f) 0 (unload).

information about structure factors or absorption, but only relative changes due to variations in local texture or variant selection.

The reference lattice parameter for each diffraction peak is obtained in a similar way, by averaging over the data set from the heat-treated sample. In addition, a correction is

made to the strains reported based on the ceria measurements. This ceria reference is used principally to correct for changes in position of the sample relative to the detector, occurring during removal and repositioning of the sample for heat treatments, or due to incrementing of the applied load. The strains reported thus should simply represent any residual or internal strains caused by the applied load or fatigue history, and will not include any influence of (initial) thermal or processing strains, since we assume these are identical for all samples and small, given the initial treatment conditions. However, given the fact that the sample has been moved in and out of the beam, there will remain a slight inherent uncertainty in the absolute strain values reported (associated with any errors in measurement of the ceria reference), which would not influence relative strain changes within a plot. Peak widths were not observed to vary more than the uncertainty in measurement in any data sets, and values are therefore not reported.

Figs. 4–9 show maps of the diffracted intensity and strain for the (0 1 0) and (1 0 0) peaks around the crack tip for the sample in the as-fatigued condition (Fig. 4) and after heat treatment under various levels of static stress intensities K_I (Figs. 5–9). Strain units are given in με (corresponding to 10^{-6} strain) and peak intensities are normalized by the reference intensity for each peak (as described above). Given a random texture for the reference sample, an intensity value of unity ($I = 1$) is expected for random orientations of grains; a value $I = 2$ means twice as many grains are oriented in this particular direction in the sample as would be expected based on random arrangements. In analogy with more formal texture analyses, units of "multiples of random distribution" (m.r.d.) are used here.

In all these figures, the nominal crack-tip position is at the origin (0,0), and the crack propagates in the positive x-direction (see Fig. 2). The crack-tip position was located by carrying out intensity scans of the sample, using the diode detector in the beam-stop, and is estimated to be correct within a 25 μm error. During the incrementing applied load stages, the nominal crack position shifted vertically (in the y-direction, due to movement of the load train as the force increases), but did not shift horizontally (in the x-direction, within measurement accuracy) except on increasing the stress intensity from 30 to 35 MPa $m^{1/2}$, when it moved by about 100 μm. This final horizontal shift is probably a result of crack growth due to the applied load.

In order of decreasing d-spacing, the (0 1 0), (0 1 1), (1 0 0), (1 1 0) and (1 0 1) diffraction peaks are all sufficiently separated to allow unambiguous high-quality peak fitting. The first four of these are indicated on Fig. 3; however, the other peaks discussed in the paper ((1 0 1), (1 1 1) and (0 0 2)) are not easily seen on the scale of the figure. Intensity and strain fields for the other measured diffraction peaks are qualitatively similar to those reported in Figs. 4–9 for (1 0 0) and (0 1 0) peaks, as illustrated in Fig. 10 for the (0 1 1), (1 1 0) and (1 0 1) peaks parallel to the loading direction for $K_I = 35$ MPa $m^{1/2}$. The (1 1 1) and (0 0 2) peaks are also sufficiently separated to provide reasonable peaks fits, but inspection of the data does not provide much additional information to that of the higher d-spacing peaks, and is not discussed here. Peak overlap among the remaining diffraction peaks means that analysis would require a Rietveld approach [42], which is beyond the scope of this paper.

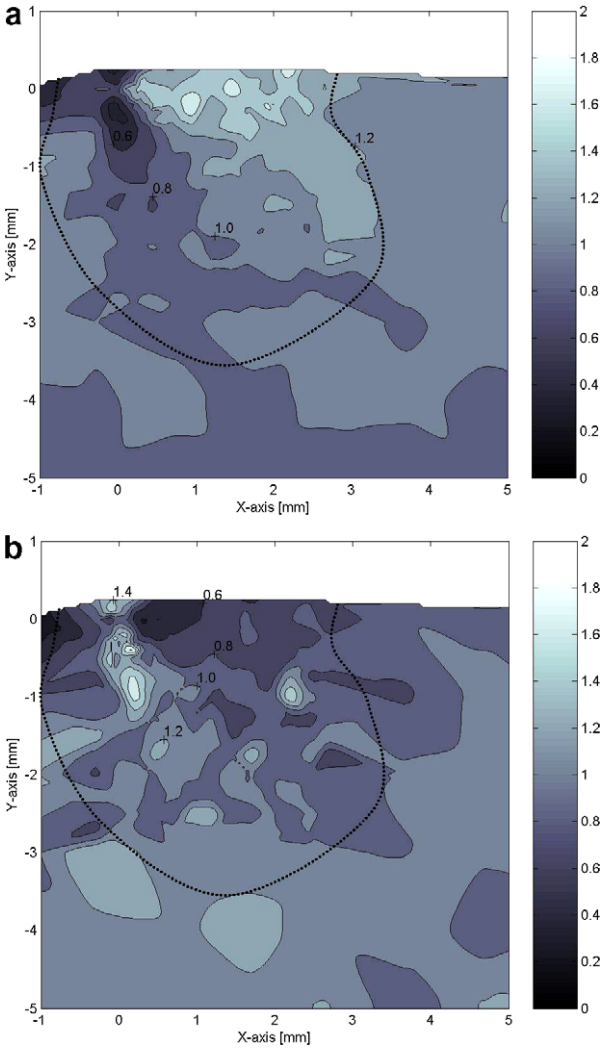

Fig. 7. Evolution of texture maps showing normalized peak intensity parallel to the x-direction (parallel to crack growth) for $K_I = 35$ MPa $m^{1/2}$. (a) (0 1 0) peak, (b) (1 0 0) peak.

4. Discussion

4.1. Residual strains and texture in as-fatigued sample

Fig. 4a and b shows maps of the normalized integrated intensities (which we can consider to be in some sense texture maps) parallel to the loading direction, obtained for the (0 1 0) and (1 0 0) peaks, respectively. With the crack tip at the origin ($x = 0$, $y = 0$), the wake of the crack is located at negative values of x, i.e. about 1 mm of the length of the fatigue formed crack is in the measurement

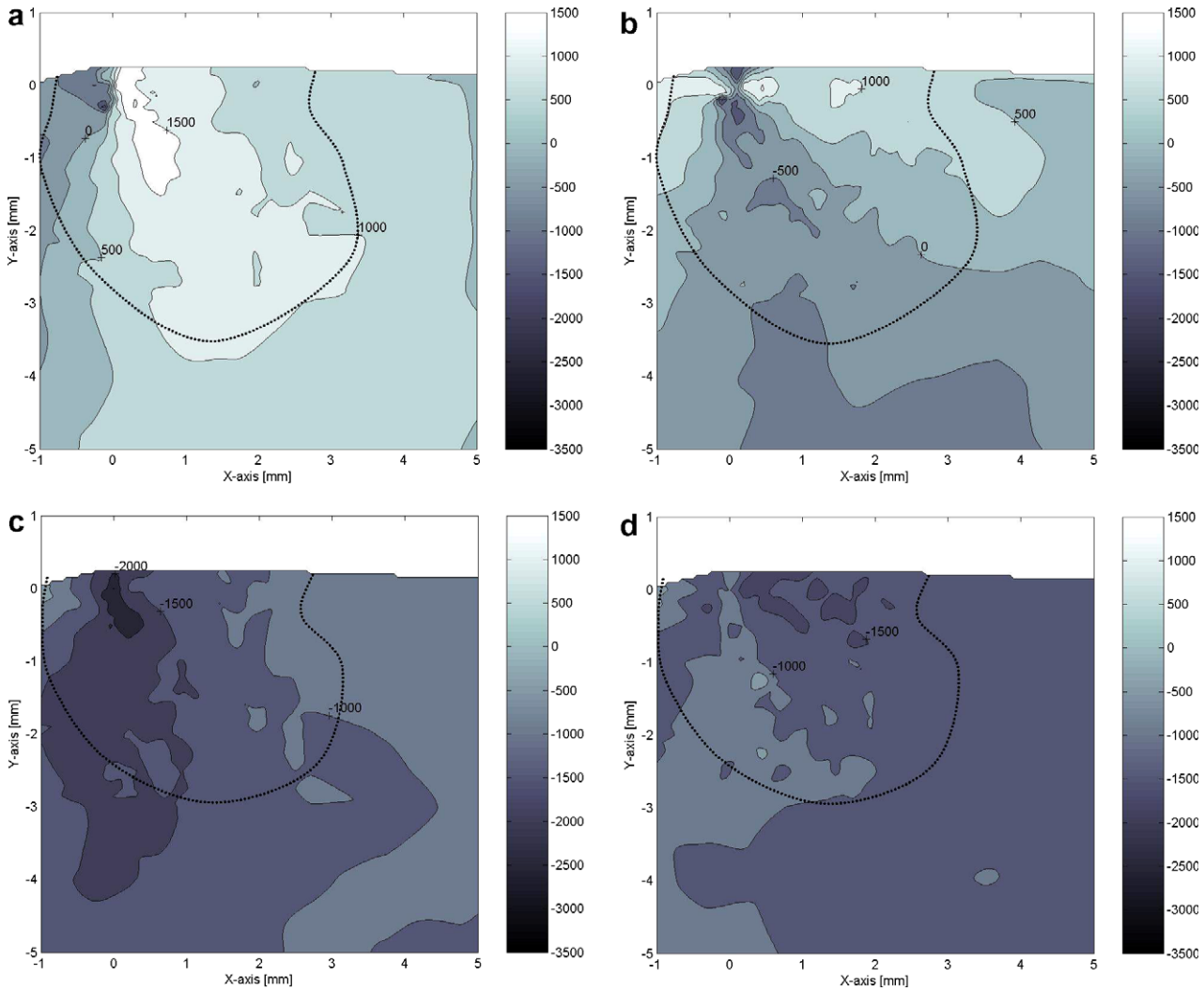

Fig. 8. Strain maps (με) for (100) peak: (a) ε_{yy} for $K_I = 35$ MPa m$^{1/2}$, (b) ε_{xx} for $K_I = 35$ MPa m$^{1/2}$, (c) ε_{yy} for $K_I =$ MPa m$^{1/2}$ (unload), (d) ε_{xx} for $K_I = 0$ MPa m$^{1/2}$ (unload).

zone. There is a strong increase in intensity for the (010) peak in the wake of the crack tip; a corresponding decrease in the intensity for the (100) peak is visible in the same areas. For comparison, an annealed, uncracked sample shows a uniform intensity value of unity, with measurement error at an individual position of approximately ±0.2, as shown in Figs. 5a and 6a. The zone of altered texture also clearly extends around 2 mm from the crack tip in the y-direction, with intensities gradually reducing from more than 2 m.r.d. near the crack tip to 1.2 m.r.d. at 2 mm for the (010) peak (i.e. corresponding to the volume fraction of grains with (010) plane normals parallel to the y-axis being around 2–1.2 times random) and correspondingly increasing from 0.5 to 0.8 m.r.d. for the (100) peak. The relative changes in intensity for the (010) and (100) peaks are thus roughly equal to each other at any given distance from the crack tip. The far field on the bottom right of the figure (for $x > 3$ and $y < -3$) represents material with random texture (intensity of 1 ± 0.2 m.r.d.), which is unaffected by the presence of the fatigue crack.

Maps of residual elastic strains determined for the same two (010) and (100) peaks are shown in Fig. 4c and d. For both peaks, the strain field in the wake of the crack shows strong residual compression (about −2000 με for (010) and −3000 με for (100)) along the y-axis, while the material far ahead of the crack ($x > 3$ and $y < -3$, with no detwinning) still shows a compressive strain but with a smaller magnitude of about −1000 με. We do not attempt here to convert the measured strains to stresses, which would necessitate knowledge of the stiffness tensor for NiTi. However, because diffraction-measured elastic strains are linearly related to stresses, qualitative comments can still be made about the stress field surrounding the crack. We note that the compressive strains, and hence stresses, near the crack tip (Fig. 4c and d) must be balanced by tensile stresses which are presumably outside of the measurement range. Also, the fact that the magnitude of residual strains (and stresses) is different for the two diffraction peaks is expected since the elastic response of NiTi is known to be strongly anisotropic [43], even without the influence of detwinning.

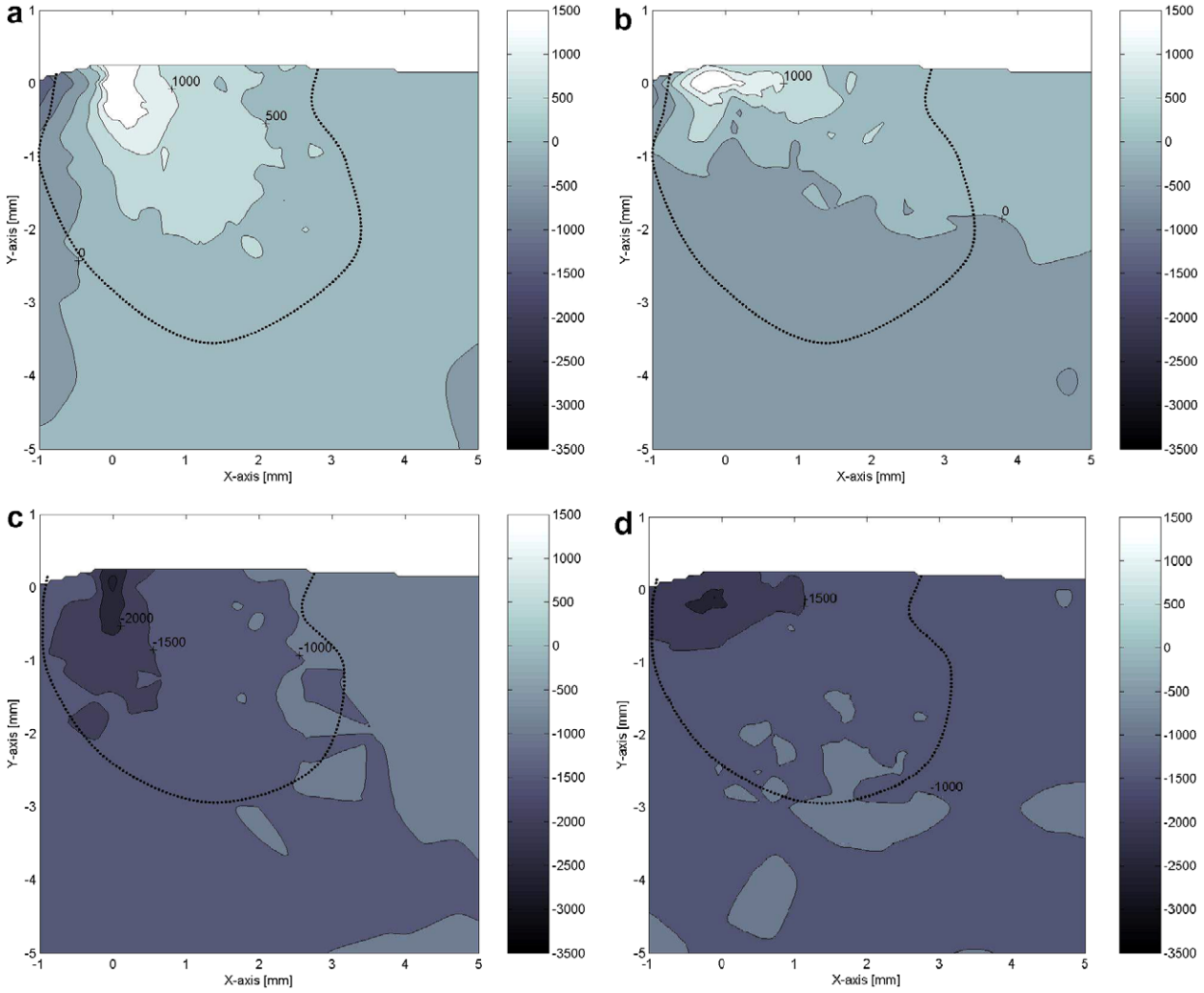

Fig. 9. Strain maps (με) for (0 1 0) peak: (a) ε_{yy} for $K_I = 35$ MPa m$^{1/2}$, (b) ε_{xx} for $K_I = 35$ MPa m$^{1/2}$, (c) ε_{yy} for $K_I = 0$ MPa m$^{1/2}$ (unload), (d) ε_{xx} for $K_I = 0$ MPa m$^{1/2}$ (unload).

It is thus apparent that fatigue crack propagation induces both substantial residual strains/stresses and texture through detwinning in the vicinity of the crack. During crack propagation, the zone ahead of the crack is expected to be in tension, with martensite detwinning acting as a deformation and relaxation mechanism, similar to the plastic zone present in metal deforming by dislocation slip. A small plastic slip zone is also probably present, but its size is expected to be much smaller than the detwinning zone, since the critical stress for slip is much higher than that for detwinning and the size of the process zone is roughly proportional to one over the square of the critical stress. Once the sample is unloaded, the volume which has deformed plastically in tension by detwinning is driven into compression by the surrounding material, possibly producing further detwinning and creating a residual strain and stress field.

Heat treatment of the fatigued sample was successful in removing any preferred orientation of the martensite variants near the crack tip, as shown in the texture maps of Figs. 5a and 6a, which is evidence that the shape-memory effect is active near the crack. This in turns confirms that the texture observed in Fig. 4a and b is indeed due to crystallographic reorientation associated with martensitic detwinning during crack propagation. The other possibility – that texture resulted from dislocation plasticity – can be discarded, since such texture would only be eliminated by a heat treatment at much higher temperatures capable of inducing recrystallization and/or grain growth.

4.2. Evolution of strains and texture in in situ tested samples

Evolution of texture is shown in Figs. 5b–e and 6b–e through normalized peak intensity maps measured under *in situ* static loading for stress intensity values $K_I = 20$, 25, 30 and 35 MPa m$^{1/2}$. The effect of increasing the applied stress intensity is clearly seen in the increase in the (0 1 0) peak intensity in the y-direction in the crack tip zone (Fig. 5b–e) and the corresponding decrease in the (1 0 0) peak intensities (Fig. 6b–e). The envelopes of the zones with intensity higher than 1.2 m.r.d. for (0 1 0) and less than 0.8 m.r.d. for (1 0 0) strongly overlap on the maps

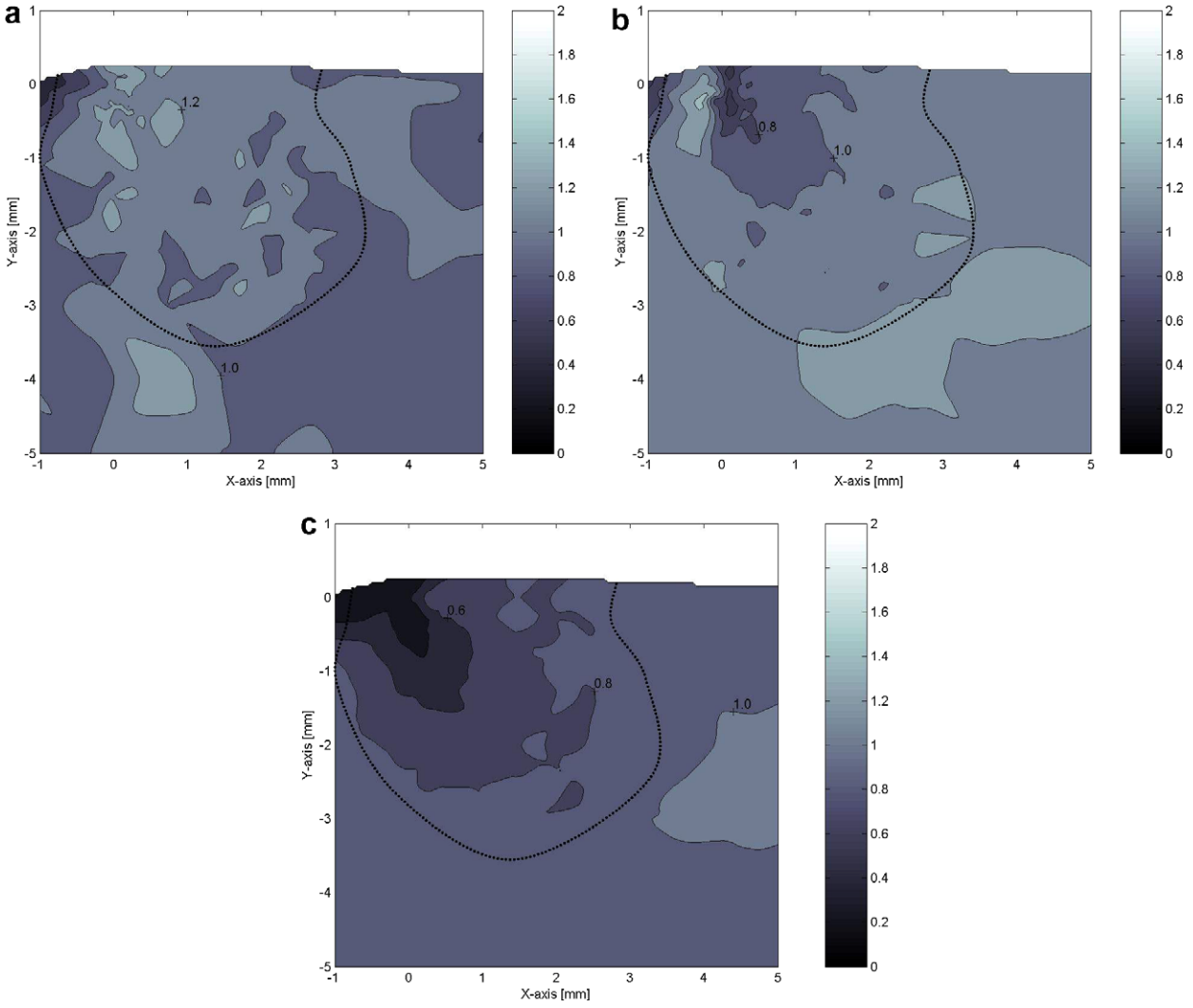

Fig. 10. Texture maps showing normalized peak intensity for $K_I = 35$ MPa $m^{1/2}$ parallel to loading direction (perpendicular to crack growth), for (a) (0 1 1) peak, (b) (1 1 0) peak and (c) (1 0 1) peak.

of Figs. 5 and 6, and hence can be taken as the extent of the detwinning zone. This zone, which is - approximately - shown as a dotted line in the maps, clearly grows with increasing applied stress. At higher levels of detwinning, the sizes of the zones appear to be slightly different in size; for example, considering the contours for 2.0 m.r.d. in Fig. 5e and 0.5 m.r.d. in Fig. 6e (which might be interpreted as about 50% of the material having detwinned), it is apparent that the latter is of larger radius, covering perhaps twice the area of the former.

In the initial phase transformation from austenite to martensite on cooling with no applied stress, there are 12 possible variants which can be formed, which are accommodated randomly in a trigonal manner [1]. As load is applied, detwinning occurs preferentially by selecting alternate variants which relax the applied stress. Given the complexity of the detwinning process (with (0 1 1), (1 1 1) and (0 0 1) "compound" twins all observed in the literature for NiTi [1]), it is not easy to make quantitative statements about the type of detwinning occurring around the crack tips. In NiTi, the *a* lattice parameter is substantially smaller than the *b* or *c* lattice parameters. Hence the observed reduction in *a* (i.e. the (1 0 0) peak in Fig. 6) intensity and increase in both the *b* (i.e. the (0 1 0) peak in Fig. 5) intensity and the *c* intensity (observed but not shown here due to space restrictions) with applied load can be understood as being driven by a detwinning stress relaxation mechanism, where an increase in the amount of "*a*"-oriented grains compared to "*b*"-oriented grains in a particular direction in the sample would act to relax compressive stress in that direction. The reverse effect would occur for tensile stresses, but in a more complex fashion, since tension can select either the "*b*"- or "*c*"-axis over the "*a*"-axis, while compression will always preferentially select the "*a*"-axis.

The change in intensities in the *x*-direction, i.e. along the crack propagation direction (shown in Fig. 7a and b for $K_I = 35$ MPa $m^{1/2}$ for the (0 1 0) and (1 0 0) peaks), displays the opposite trend to that seen in the *y*-direction (shown in Figs. 5e and 6e), with – in general – locations of reduced intensity in the *y*-direction corresponding to locations of increased intensity in the *x*-direction for a given diffraction peak and vice versa. However, some deviations from this

simple rule are observed, most probably due to the complex multi-axial stress field.

The maximum normalized intensities in the y-direction observed at $K_I = 35$ MPa m$^{1/2}$ were ~3.5 m.r.d. for the (0 1 0) and ~0.1 m.r.d. for the (1 0 0) peaks, which are not shown on the corresponding figures (Figs. 5e and 6e, respectively) due to the contour levels chosen. Even without considering the twinning mechanisms and the details of the monoclinic crystal structure, these differences in the maximum intensities, as well as in the extent of the nominal 50% twinning level described above, can be roughly understood in terms of the symmetry of the crystal structure discussed in the previous paragraph. If a tensile stress causes a grain with the (1 0 0) axis in a given direction to detwin, it can select twins that tend to have either a "b" or "c"-axis (or intermediate) in the tensile stress direction. Thus, even though there is a large reduction in the number of grains with the (1 0 0) peak in a given direction, there is a smaller relative increase in the number of grains with the (0 1 0) peak in that direction, since there will also be some grains detwinning to other orientations.

For $K_I = 0$ MPa m$^{1/2}$ after unloading from $K_I = 35$ MPa m$^{1/2}$ (Figs. 5f and 6f), there is a very slight reversal of detwinning compared to that seen at maximum load (Figs. 5e and 6e), but the majority of the detwinning is permanent.

The extent of the detwinned zone (delineated in Figs. 5e and 6e, as described above) can be compared to the prediction from linear elastic fracture mechanics (LEFM). Using the standard equations for stress at a crack tip in the absence of any relaxation mechanism (as given e.g. in Ref. [44]), it is possible to calculate the elastic strain or von Mises equivalent stress as a function of distance and angle from the crack tip. Fig. 11a–c shows the results from such calculations carried out in MATLAB [39] under plane-strain assumptions with a Young's modulus of 62 GPa and Poisson ratio of 0.3 [16] for a stress intensity $K_I = 35$ MPa m$^{1/2}$. By comparing Fig. 11c with Figs. 5e and 6e, it can be seen that the envelope of the detwinned zone corresponds roughly to a von Mises stress of 200 MPa, which is in reasonable agreement with the values reported for the uniaxial applied stress required to cause detwinning in NiTi

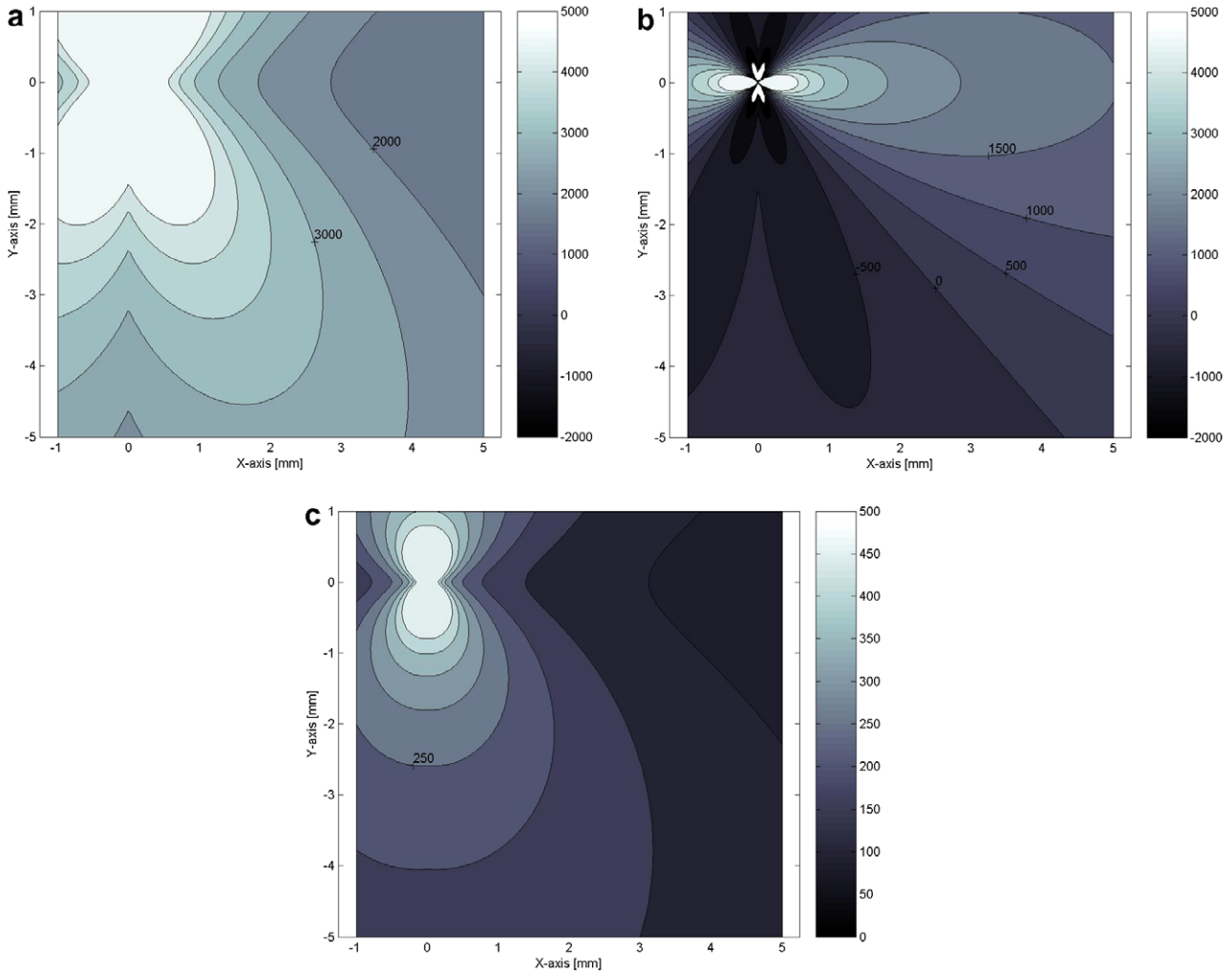

Fig. 11. Linear elastic fracture mechanics predictions (assuming plane strain) for $K_I = 35$ MPa m$^{1/2}$. (a) Elastic strain parallel to loading direction ε_{yy} (με); (b) elastic strain perpendicular to loading direction ε_{xx} (με); (c) von Mises effective stress (MPa).

(e.g. [34]). More quantitative comparisons are not possible using this approach, given the ambiguities in comparing an LEFM calculation (Fig. 11a–c) with the present measurements of inelastic deformation by detwinning (Figs. 5e and 6e). More complex numerical modeling techniques (e.g. finite element models) would be required to allow a more quantitative comparison in terms of the shape of the detwinning zone and its evolution with increasing stress (e.g. [16]), and will be the subject of future work.

Maps of elastic strains are shown for the maximum applied load ($K_I = 35$ MPa $m^{1/2}$) for the (100) peak (Fig. 8a and b) and the (010) peak (Fig. 9a and b) both perpendicular (y-axis) and parallel (x-axis) to the crack propagation direction. High tensile ε_{yy} strains are seen in the zone close to the crack tip, with maxima of 2400 με in the (100) peak (Fig. 8a) and 3200 με in the (010) peak (Fig. 9a). Ahead of the crack tip (i.e. $y \sim 0$, $x > 0.2$), strains are highly triaxial in nature, with tensile strains for both ε_{xx} and ε_{yy} (Figs. 8a and b and 9a and b). The elastic ε_{yy} strains observed in the (100) peak (Fig. 8a) further from the crack tip are generally more tensile than the strains seen in the (010) peak (Fig. 9a), as expected from the elastic anisotropy of NiTi. For the ε_{xx} strains, the effects of the crystallography appear to be more significant with the (100) grains (Fig. 8b) in compression very close to the crack tip (0 με at the crack tip itself, increasing in magnitude to −1000 με at 0.2 mm from the tip), while the (010) grains are in tension (with a peak of approximately 2000 με). These maps are in qualitative (though not quantitative, as expected) agreement with LEFM calculations of strain (Fig. 11a and b). For example, the compressive "lobe" in the ε_{xx} strains seen extending at about 60° from the crack propagation direction (Fig. 8b) is predicted by LEFM (Fig. 11b). Again, the elastic anisotropy is clear, with the (100) grains (Fig. 8b) showing significantly larger magnitude compressive strains in this region than seen for the (010) grains (Fig. 9b).

Finally, after unloading (Figs. 8c and d, 9c and d), the entire residual strain fields for the (100) and (010) peaks are compressive, with greatest compression seen near the crack tip reaching maximum ε_{yy} strains of about −2500 με for both the (100) and (010) peaks. Slightly smaller magnitude compressive ε_{xx} strains are seen. This strain field is similar to, but perhaps more clearly defined than, the residual strain field observed around the unloaded crack after fatigue propagation (Fig. 4c and d). The similarity is expected since in both cases crack propagation occurred, although during fatigue and static loading, respectively.

5. Conclusions

Two-dimensional maps of elastic strain and texture (averaged through the specimen thickness) in the vicinity of a crack tip in a martensitic NiTi alloy were created from *in situ* synchrotron X-ray diffraction measurements. The following results were obtained:

- After fatigue crack propagation with $\Delta K_I = 30$ MPa $m^{1/2}$, the material in the vicinity of the crack and in its wake exhibits texture and residual compressive strains.
- A shape-memory recovery heat treatment eliminates this texture, indicating that it is due to detwinning, the main deformation mechanism of NiTi.
- Static tensile loading of the sharp fatigue crack leads to reappearance of the textured zone around the crack tip, and its growth as the stress is incrementally increased. This detwinning zone is similar to the plastic zone produced by dislocation slip present around cracks in other metals.
- Under the highest applied stress intensity $K_I = 35$ MPa $m^{1/2}$, high triaxial tensile strains are measured within and beyond the detwinning zone around the crack tip, with this strain field becoming compressive when the applied stress is removed. The elastic anisotropy of NiTi is apparent in the complex distribution of strain for different diffraction peaks.
- Mechanical unloading of the crack does not alter the texture of the detwinned zone near the crack tip, but produces considerable compressive residual strains.

Acknowledgements

Use of the Advanced Photon Source was supported by the US Department of Energy, Office of Science, Office of Basic Energy Sciences, under Contract No. DE-AC02-06CH11357 is supported by the Natural Sciences and Engineering Research Council of Canada. D.C.D. acknowledges support from the US National Science Foundation through Grant DMR-0505772/001.

References

[1] Otsuka K, Wayman CM. Shape memory materials. London: Cambridge University Press; 1998.
[2] Otsuka K, Ren X. Recent developments in the research of shape memory alloys. Intermetallics 1999;7(5):511–28.
[3] Shabalovskaya S. On the nature of the biocompatibility and on medical applications of NiTi shape memory and superelastic alloys. Bio-Med Mater Eng 1996;6(4):267–89.
[4] Thompson S. An overview of nickel–titanium alloys used in dentistry. Int Endod J 2000;33(4):297–310.
[5] Shabalovskaya S. Surface, corrosion and biocompatibility aspects of Nitinol as an implant material. Bio-Med Mater Eng 2002;12(1):69–109.
[6] Haikel Y, Serfaty R, Bateman G, Senger B, Allemann C. Dynamic and cyclic fatigue of engine-driven rotary nickel–titanium endodontic instruments. J Endodont 1999;25(6):434–40.
[7] Gall K, Yang N, Sehitoglu H, Chumlyakov YI. Fracture of precipitated NiTi shape memory alloys. Int J Fracture 2001;109(2):189–207.
[8] McKelvey AL, Ritchie RO. Fatigue-crack growth behavior in the superelastic and shape-memory alloy Nitinol. Metall Mater Trans A 2001;32(3A):731–43.
[9] Eggeler G, Hornbogen E, Yawny A, Heckmann A, Wagner M. Structural and functional fatigue of NiTi shape memory alloys. Mater Sci Eng A 2004;378(1–2):24–33.
[10] Hornbogen E, Eggeler G. Surface aspects in fatigue of shape memory alloys (SMA). Materialwiss Werkst 2004;35(5):255–9.
[11] Chen J, Sun W, Wang G. Investigation on the fracture behavior of shape memory alloy NiTi. Metall Mater Trans A 2005;36(4):941–55.

[12] Kasuga J, Yoneyama T, Kobayashi E, Hanawa T, Doi H. Fatigue property of super-elastic Ti–Ni alloy dental castings. Mater Trans 2005;46(7):1555–63.
[13] Matsui R, Makino Y, Tobushi H, Furuichi Y, Yoshida F. Influence of strain ratio on bending fatigue life and fatigue crack growth in TiNi shape-memory alloy thin wires. Mater Trans 2006;47(3):765–9.
[14] Yan WY, Wang CH, Zhang XP, Mai YW. Effect of transformation volume contraction on the toughness of superelastic shape memory alloys. Smart Mater Struct 2002;11(6):947–55.
[15] Wang XM, Wang YF, Baruj A, Eggeler G, Yue ZF. On the formation of martensite in front of cracks in pseudoelastic shape memory alloys. Mater Sci Eng A 2005;394(1–2):309–93.
[16] Wang GZ. Effects of notch geometry on stress–strain distribution martensite transformation and fracture behavior in shape memory alloy NiTi. Mater Sci Eng A 2006;434:269–79.
[17] Dunand DC, Mari D, Bourke MAM, Goldstone JA. NiTi and NiTi–TiC composites. Part IV. neutron diffraction study of twinning and shape-memory recovery. Metall Mater Trans A 1996;27:2820–36.
[18] Vaidyanathan R, Dunand DC, Ramamurty U. Fatigue crack-growth in shape-memory NiTi and NiTi–TiC composites. Mater Sci Eng A 2000;289(1–2):208–16.
[19] Schuster A, Voggenreiter HF, Dunand DC, Eggeler G. A new type of intrinsic two-way shape-memory effect in hooks of NiTi-wires. J Phys IV 2003;112(2):1177–80.
[20] Rathod CR, Rajagopalan S, Vaidyanathan R. Mechanical characterization of Shape-memory alloys using diffraction and instrumented indentation. In: Shape-memory and Superelastic Technologies 2003, International Organization on Shape-Memory and Superelastic Technologies; 2004. p. 331–9.
[21] Bourke MAM, Vaidyanathan R, Dunand DC. Neutron diffraction measurement of stress-induced transformation in superelastic NiTi. Appl Phys Lett 1996;69(17):2477–9.
[22] Vaidyanathan R, Bourke MAM, Dunand DC. Phase fraction, texture and strain evolution in superelastic NiTi and NiTi–TiC composites investigated by neutron diffraction. Acta Mater 1999;47(12):3353–66.
[23] Vaidyanathan R, Bourke MAM, Dunand DC. Analysis of neutron diffraction spectra acquired in situ during stress-induced transformations in superelastic NiTi. J Appl Phys A 1999;86(6):3020–9.
[24] Sitepu H, Klonne M, Schmahl WW, Predki W, Pirling T. Measurements of strain, texture and phase fraction in aged Ni-rich NiTi shape memory alloys by neutron powder diffraction technique under in situ torsional loading. J Phys IV 2003;112(2):811–4.
[25] Šittner P, Lukáš P, Novák V, Daymond MR, Swallowe GM. In situ neutron diffraction studies of martensitic transformation in NiTi polycrystals under tension and compression stress. Mater Sci Eng A 2004;378:97–104.
[26] Khalil-Allafi J, Hasse B, Klonne M, Wagner M, et al. In situ diffraction investigation of superelastic NiTi shape memory alloys under mechanical stress with neutrons and with synchrotron radiation. Materialwiss Werkst 2004;35(5):280–3.
[27] Lai BK, Kahn H, Phillips SM, Akase Z, Heuer AH. Quantitative phase transformation behavior in TiNi shape memory alloy thin films. J Mater Res 2004;19(10):2822–33.
[28] Rathod CR, Clausen B, Bourke MAM, Vaidyanathan R. Neutron diffraction investigation of hysteresis reduction and increase in linearity in the stress–strain response of superelastic NiTi. Appl Phys Lett 2006;88(20):201919.
[29] Mehta A, Gong X-Y, Imbeni V, Pelton AR, Ritchie RO. Understanding the deformation and fracture of Nitinol endovascular Stents using in situ synchrotron X-ray micro-diffraction. Adv Mater 2007;19:1183–86, doi:10.1002/adma.200601916.
[30] James MN, Hattingh DG, Hughes DJ, Wei L-W, Patterson EA, Fonseca JQD. Synchrotron diffraction investigation of the distribution and influence of residual stresses in fatigue. Fatigue Fract Engng Mater Struct 2004;27:609–22.
[31] Steuwer A, Edwards L, Pratihar S, Ganguly S, Peel M, Fitzpatrick ME, et al. In situ analysis of cracks in structural materials using synchrotron X-ray tomography and diffraction. Nuc Inst & Methods in Phys Res B 2006;246:217–25.
[32] Croft M, Zhong Z, Jisrawi N, Zakharchenko I, Holtz RL, Skaritka J, et al. Strain profiling of fatigue crack overload effects using energy dispersive X-ray diffraction. Int J Fatigue 2005;27:1408–19.
[33] Marrow TJ, Steuwer A, Mohammed F, Engelberg D, Sarwar M. Measurement of crack bridging stresses in environment-assisted cracking of duplex stainless by synchrotron diffraction. Fatigue Fract Engng Mater Struct 2006;29:464–71.
[34] Johansen K, Voggenreiter H, Eggeler G. On the effect of TiC particles on the tensile properties and on the intrinsic two way effect of NiTi shape memory alloys produced by powder metallurgy. Mater Sci Eng A 1999;275(S1):410–4.
[35] Daymond MR, Withers PJ. A synchrotron radiation study of transient internal strain changes during the early stages of thermal cycling in an Al/SiC_w MMC. Scripta Mater 1996;35(10):1229–34.
[36] Wanner A, Dunand DC. Synchrotron X-ray study of bulk lattice strains in externally loaded Cu–Mo composites. Metall Mater Trans A 2000;31(11):2949–62.
[37] Young ML, Almer JD, Daymond MR, Haeffner DR, Dunand DC. Load partitioning between ferrite and cementite during elasto-plastic deformation of an ultrahigh-carbon steel. Acta Mater 2007;55(6):1999–2001.
[38] He BB, Smith KL. In: SEM Spring conference on experimental and applied mechanics and experimental/numerical mechanics in electronic packaging III, Houston, TX; 1998.
[39] MATLAB. Available from: www.mathworks.com.
[40] Hammersley AP. FIT2D V9.129 reference manual V3.1, ESRF internal report; 1998.
[41] Larson AC, Von Dreele RB. GSAS – general structure analysis system. Los Alamos (NM): Los Alamos National Laboratory; 1994.
[42] Rietveld HM. A profile refinement method for nuclear and magnetic structures. J Appl Crystallogr 1969;2:65–71.
[43] Vaidyanathan R, Bourke MAM, Dunand DC. Texture, strain, and phase-fraction measurements during mechanical cycling in superelastic NiTi. Metall Mater Trans A 2001;32:777–86.
[44] Anderson TL. Fracture mechanics: fundamentals and applications. 2nd ed. Boca Raton (FL): CRC Press; 2005, ISBN 0849316561.